Iodinated gadolinium-gold nanomaterial as a multimodal contrast agent for cartilage tissue imaging

Cite as: APL Bioeng. **8**, 036110 (2024); doi: 10.1063/5.0215273
Submitted: 23 April 2024 · Accepted: 29 July 2024 ·
Published Online: 19 August 2024

View Online Export Citation CrossMark

Cheng-Hsiu Lu,[1,2,3] Wei-Shiung Lian,[1,2,3,4] Re-Wen Wu,[3,5] Yu-Han Lin,[2,3,4] Chia-Hao Su,[6,7,8,9] Chuan-Lin Chen,[9] Ming-Hong Tai,[10] Yu-Shan Chen,[1,2,3,4] Shao-Yu Wang,[1,2,3,4] Chao-Cheng Chen,[11] and Feng-Sheng Wang[1,2,3,4,a)]

AFFILIATIONS

[1]Core Laboratory for Phenomics & Diagnostics, Kaohsiung Chang Gung Memorial Hospital, Kaohsiung 833, Taiwan
[2]Department of Medical Research, Kaohsiung Chang Gung Memorial Hospital, Kaohsiung 833, Taiwan
[3]Department of Medicine, Graduate Institute of Clinical Medical Sciences, Chang Gung University College of Medicine, Kaohsiung 833, Taiwan
[4]Center for Mitochondrial Research and Medicine, Kaohsiung Chang Gung Memorial Hospital, Kaohsiung 833, Taiwan
[5]Department of Orthopedic Surgery, Kaohsiung Chang Gung Memorial Hospital, Kaohsiung 833, Taiwan
[6]Department of Radiation Oncology, Kaohsiung Chang Gung Memorial Hospital, Kaohsiung 833, Taiwan
[7]Center for General Education, Chang Gung University, Taoyuan 333, Taiwan
[8]Institute for Radiological Research, Chang Gung University, Taoyuan 333, Taiwan
[9]Department of Biomedical Imaging and Radiological Sciences, National Yang Ming Chiao Tung University, Taipei 112, Taiwan
[10]Institute of Biomedical Sciences, National Sun Yat-sen University, Kaohsiung 804, Taiwan
[11]Department of Molecular Oncology, BC Cancer Research Institute, Vancouver, British Columbia V5Z1L3, Canada

[a)]**Author to whom correspondence should be addressed:** wangfs@ms33.hinet.net

ABSTRACT

Cartilage damage, a common cause of osteoarthritis, requires medical imaging for accurate diagnosis of pathological changes. However, current instruments can acquire limited imaging information due to sensitivity and resolution issues. Therefore, multimodal imaging is considered an alternative strategy to provide valuable images and analyzes from different perspectives. Among all biomaterials, gold nanomaterials not only exhibit outstanding benefits as drug carriers, *in vitro* diagnostics, and radiosensitizers, but are also widely used as contrast agents, particularly for tumors. However, their potential for imaging cartilage damage is rarely discussed. In this study, we developed a versatile iodinated gadolinium-gold nanomaterial, AuNC@BSA-Gd-I, and its radiolabeled derivative, AuNC@BSA-Gd-^{131}I, for cartilage detection. With its small size, negative charge, and multimodal capacities, the probe can penetrate damaged cartilage and be detected or visualized by computed tomography, MRI, IVIS, and gamma counter. Additionally, the multimodal imaging potential of AuNC@BSA-Gd-I was compared to current multifunctional gold nanomaterials containing similar components, including anionic AuNC@BSA, AuNC@BSA-I, and AuNC@BSA-Gd as well as cationic AuNC@CBSA. Due to their high atomic numbers and fluorescent emission, AuNC@BSA nanomaterials could provide fundamental multifunctionality for imaging. By further modifying AuNC@BSA with additional imaging materials, their application could be extended to various types of medical imaging instruments. Nonetheless, our findings showed that each of the current nanomaterials exhibited excellent abilities for imaging cartilage with their predominant imaging modalities, but their versatility was not comparable to that of AuNC@BSA-Gd-I. Thus, AuNC@BSA-Gd-I could be served as a valuable tool in multimodal imaging strategies for cartilage assessment.

I. INTRODUCTION

Cartilage is a type of fibrous connective tissue that functions as a smooth and lubricated surface, enabling joints to move with minimal friction.[1] Once cartilage is damaged by persistent physical loading, trauma, or autoimmune responses, diseases such as osteoarthritis (OA) or rheumatoid arthritis (RA) may occur. To diagnose cartilage disorders, medical imaging strategies are widely used to detect lesions on the cartilage. However, current imaging modalities have limitations in directly visualizing cartilage due to insufficient resolution and sensitivity, necessitating the development of contrast agents. Anionic ioxaglate (Hexabrix^{TM} 320), cationic CA4^{+}, and anionic gadopentetate dimeglumine (Gd-DTPA^{2-}) could be used to evaluate cartilage degradation through contrast-enhanced computed tomography (CECT) or delayed gadolinium-enhanced MRI of cartilage (dGEMRIC). However, their clinical efficacy is still being evaluated, and *in vivo* side effects have been noted.[2–4] Sulfated glycosaminoglycans (sGAGs), abundant in sulfate groups such as carboxylic acid, result in a highly negative charge on the GAG molecules.[5] With approximately 20% occupancy in cartilage,[6] sGAGs have been recognized as targeting molecules that could provide significant imaging enhancement. Therefore, current contrast agents are developed based on the charged attraction or repulsion between ionic agents and the negative sGAG in cartilage. Nanomaterial-based contrast agents might be the promising candidates due to their adjustable charge, size, and modifiability. In our hypothesis, any ionic nanomaterials with imaging functionalities have the potential to visualize articular cartilage by targeting negatively charged sGAG chain.

However, discussion of nanomaterial-based cartilage contrast agents has been limited to date, primarily due to the constrained pore size of the proteoglycan network, which measures 20 nm and restricts the effective penetration of larger nanomaterials into cartilage.[7] The Au@PDA-WL NPs, a gold nanomaterial-based photoacoustic imaging probe, were verified to diagnose early OA. However, the study adopted an active delivery strategy by modifying WYRGRL to NPs to target the collagen II peptide. Despite achieving effective diagnosis, the cost and synthesis difficulty hinder the possibility of widespread use. Several nanoparticle-based materials, such as tantalum oxide, ioxaglate (IOX), and poly-l-lysine melanin nanoparticles, relying on passive electrostatic interactions for targeting, have been utilized to monitor damaged cartilage using unimodal imaging modalities like computed tomography (CT) or photoacoustic imaging.[8–11] In comparison, the passive targeting strategy is more applicable for developing a cartilage imaging probe for widespread use.

Current imaging techniques like CT, MRI, and sonography offer precise anatomical resolution but often lack the sensitivity needed to detect functional changes. Conversely, nuclear and optical imaging allow for the visualization of molecular changes but may require additional equipment to overcome resolution limitations.[12–14] Therefore, there is an urgent need to develop multimodal imaging probes to assess pathological changes in lesions from different perspectives. Multimodal imaging techniques have been reported to enhance diagnostic capabilities for cancers, atherosclerosis, and neuropsychiatric disorders, and to accelerate pre-clinical research and clinical practice.[15,16] While extensive efforts are under way to develop multimodal imaging probes, their efficacy for cartilage imaging remains uncertain. For instance, bismuth nanoparticles (BiNPs) were reported to be combined with gadolinium-diethylenetriaminepentaacetic acid-bis-tetradecylamide to synthesize Gd-PEG-Bi NPs for triple-modal imaging (MRI/CT/photoacoustic imaging).[17] However, the hydrodynamic radius of these NPs was relatively large, potentially hindering diffusion into cartilage tissue. Therefore, the search for suitable materials to develop effective multimodal imaging probes for cartilage should continue.

Fluorescent gold nanoclusters protected by bovine serum albumin (AuNC@BSA) are synthesized using an environmentally friendly process involving BSA-mediated reduction and stabilization.[18,19] These nanoclusters have the potential to serve various purposes, such as drug carriers, imaging probes, and biosensors, and can be utilized in therapeutic strategies, including chemotherapy, photothermal therapy (PTT), and photodynamic therapy (PDT).[20–22] Due to their high atomic number and fluorescence characteristics, gold nanoclusters are appropriate as cores for developing multimodal imaging probes, especially for cartilage, owing to their small size and flexible charges. Herein, we synthesized an innovative multifunctional iodinated gadolinium-gold nanomaterial (AuNC@BSA-Gd-I) along with its radioactive derivative, AuNC@BSA-Gd-^{131}I. Owing to their small size and modifications, the probes might enable multimodal visualization and quantification of defective cartilage using optical imaging, MRI, CT, and gamma counters. Given their anionic properties, the imaging intensity of cartilage generated by AuNC@BSA-Gd-I is likely to show an inverse correlation with sGAG content. Nevertheless, many current anionic and cationic gold-based nanomaterials have been developed. Once the particle size is smaller than 20 nm, they might serve as candidates for cartilage imaging. Therefore, we selected candidate nanomaterials that have demonstrated their multimodal imaging potentials in other studies to examine their abilities for cartilage imaging, subsequently comparing their abilities and versatility in visualizing cartilage tissue to AuNC@BSA-Gd-I. Our findings indicate that while these nanomaterials could serve as unimodal or dual-modal imaging probes for cartilage, their potential for multimodal visualization is limited. This suggests that AuNC@BSA-Gd-I exhibits superior application and versatility for cartilage imaging (Fig. 1).

II. RESULTS AND DISCUSSION

A. Physicochemical characterization of AuNC@BSA-Gd-I

Owing to its eco-friendly and facile production process, the synthesis, characterization, and quantification of AuNC@BSA-Gd-I can be easily accomplished in basic biology laboratories (Fig. S1). Unlike larger gold nanoparticles, nanoclusters smaller than 3 nm do not exhibit the surface plasmon resonance (SPR) effect, and, consequently, no distinct SPR absorption peak was detected via UV-vis. However, an apparent I^{-} characteristic absorption was observed at approximately 225 nm.[23–25] The AuNC@BSA-Gd-I exhibited excitation and emission peaks at 470 and 640 nm, respectively [Fig. 2(a)], appearing brown in visible light and red under 365 nm UV light [Fig. 2(b)]. The AuNC@BSA-Gd-I appeared smaller than 5 nm in TEM images, displaying a spherical morphology [Fig. 2(c)]. Additionally, AuNC@BSA-Gd-I exhibited a small hydrodynamic radius with a peak at 8.05 ± 2.43 nm and a zeta potential of -13.5 ± 1.18 mV [Fig. 2(d)]. With its small size and anionic properties, AuNC@BSA-Gd-I might effectively penetrate cartilage tissue and preferentially accumulate in regions with higher sGAG content. In addition, the stability of iodine and gadolinium binding was assessed using UV-vis and MRI analysis.

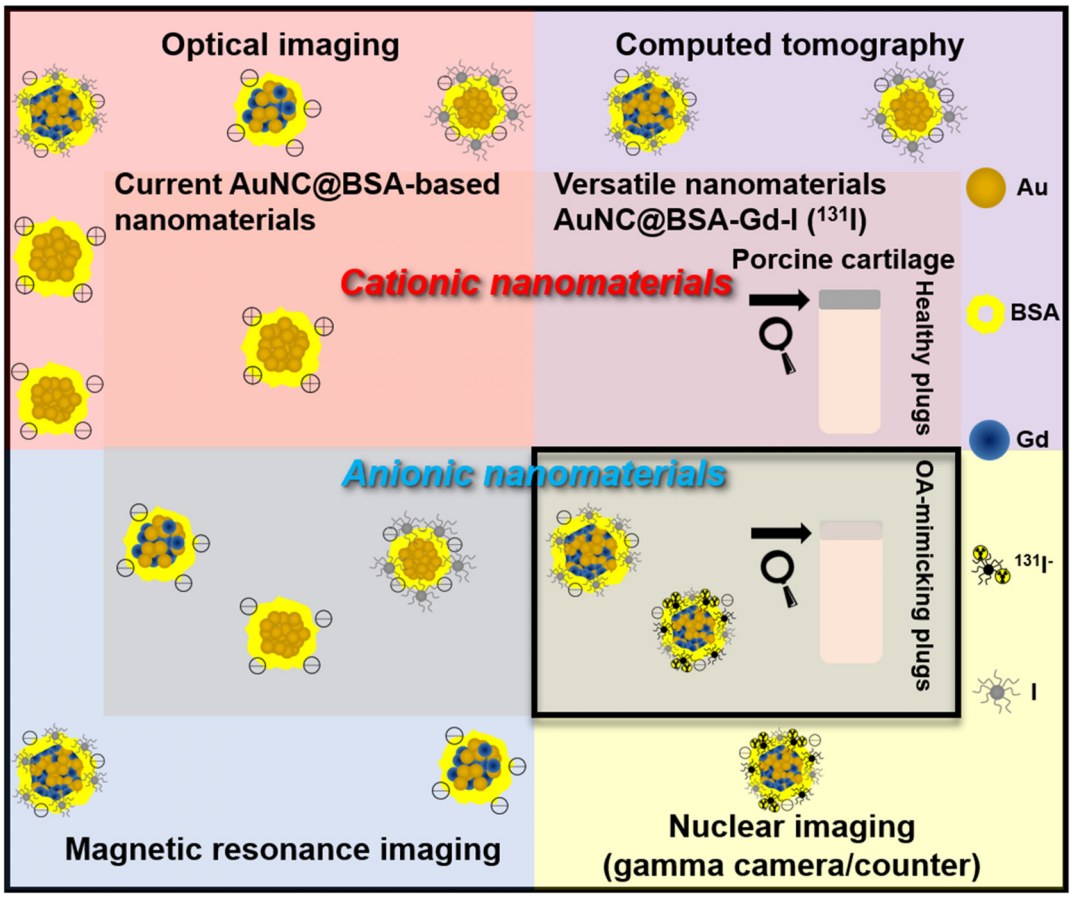

FIG. 1. Schematic illustration comparing the versatility of AuNC@BSA-Gd-I for cartilage imaging and detection with current gold nanomaterials.

The results showed stable iodine modification for up to 24 h in fetal bovine serum (FBS) (81.89 ± 0.03%) or phosphate-buffered saline (PBS) (96.5 ± 0.04%), and robust gadolinium conjugation for up to 24 h in FBS (86.9 ± 0.28%) or PBS (86.08 ± 0.86%) [Fig. 2(e)]. The iodine labeling yield of AuNC@BSA-Gd-I was 90.73 ± 0.35%.

B. Imaging potential of AuNC@BSA-Gd-I for MRI and CT

Due to the inclusion of Gd and I, which are common materials used to enhance contrast in MRI and CT images, the abilities of AuNC@BSA-Gd-I nanomaterials as contrast agents for MRI and CT were assessed. Longitudinal (T1) relaxation times were acquired across concentrations ranging from 0.625 mg/ml (0.018 mg Gd/ml) to 5 mg/ml (0.07 mg Gd/ml). The T1-weighted images showed enhanced contrast after modification with Gd, and the r1 value of 0.98 s^{-1} per mg/ml (coefficient of determination, $R^2 = 0.99$, $P < 0.0001$) of BSA concentration in distilled water was calculated. However, visualization became difficult when the dose decreased to 0.625 mg/ml [Figs. 3(a) and 3(b)]. Due to the k-edge of iodine being at 33.2 keV, appropriate kVp values would bring the energy exposure of AuNC@BSA-Gd-I closer to its k-edge, resulting in stronger x-ray attenuation.[26] However, depending on the instrument, objects are typically exposed to x rays with an average energy that is usually 1/3 to 1/2 of the maximum energy.[27] Therefore, the settings of 60 and 90 kVp were used in CT imaging and analysis. According to the CT analysis, the attenuation generated by 20 mg/ml (0.838 mg I/ml) AuNC@BSA-Gd-I was 1948.68 ± 9.9 Hounsfield Units (HU) at 90 kVp ($R^2 = 0.99$, $P < 0.0001$) and 1624.12 ± 16.57 HU at 60 kVp ($R^2 = 0.99$, $P < 0.0001$), suggesting the potential of the AuNC@BSA-Gd-I as a CT contrast agent for cartilage assessment [Figs. 3(c), 3(d), and S2].

C. Visualization and analysis of cartilage following AuNC@BSA-Gd-I accumulation via MRI and CT

Given that the cartilage in small animals is much thinner than in humans, which poses challenges for the detection using current instruments and presents obstacles in proving our hypothesis, we employed an *in vitro* porcine model. The model involved extracting cartilage plugs from porcine knee joint and treating them with trypsin to induce early OA.[28–30] Before conducting imaging studies of the cartilage, the cationic dye safranin O was utilized to examine the efficiency of sGAG content degradation [Fig. S3(a)]. The results revealed that healthy plugs (control) exhibited abundant accumulation of safranin O at the cartilage portion, attributed to electrostatic interactions [Fig. S3(b)]. In contrast, OA-mimicking plugs treated with trypsin encountered

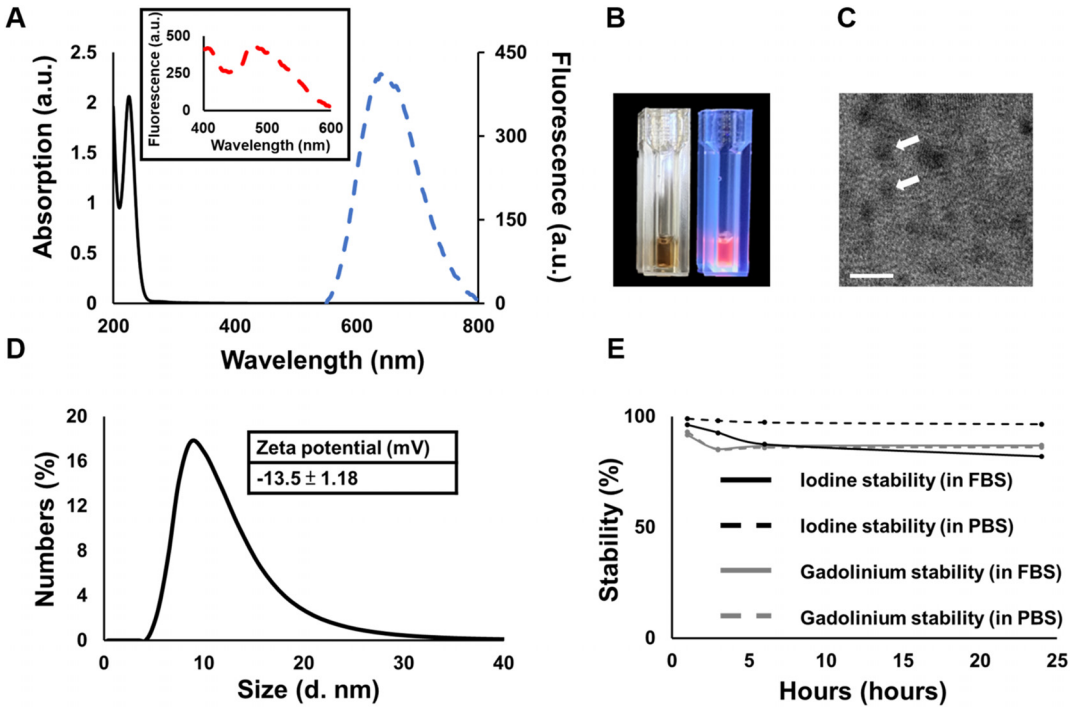

FIG. 2. Characterization of AuNC@BSA-Gd-I. (a) The absorption values were merged with the fluorescent emission spectrum, and the inset figure displayed the spectrum of fluorescent excitation. Black line, UV-vis spectra; blue dotted line, emission spectra ($\lambda_{ex} = 470$ nm); red dotted line, excitation spectra ($\lambda_{em} = 640$ nm). (b) The AuNC@BSA-Gd-I exhibited red fluorescence under UV light (365 nm). (c) The exact size and morphology of AuNC@BSA-Gd-I were observed using TEM. The scale bars are 5 nm. (d) The hydrodynamic radius of AuNC@BSA-Gd-I was recorded, and an inner table displayed the zeta potential. (e) Quantitative UV-vis spectrum and MRI analysis were employed to calculate the stability of iodine and gadolinium contained in AuNC@BSA-Gd-I when exposed to PBS or FBS for 1, 3, 6, and 24 h after modification.

difficulties in observing staining in the cartilage area due to the loss of sGAG content [Fig. S3(c)]. An additional advantage of the model is that the animals are obtained from a local slaughterhouse, aligning with the principle of "Replacement" within the 3Rs (Refinement, Reduction, Replacement).[31]

The ability of AuNC@BSA-Gd-I to detect damaged cartilage was assessed using small animal MRI and CT. To comply with laboratory regulations and for scanning convenience, the cartilage portions of the plugs containing AuNC@BSA-Gd-I were excised after 24 h of incubation, dissolved in papain reagent, and then subjected to MRI analysis. T1-weighted MRI scans of cartilage containing AuNC@BSA-Gd-I showed cartilage enhancement [Fig. 3(e)], with signal intensities collected at 24 h post-incubation exhibiting an inverse correlation with sGAG content ($R^2 = 0.93$, $P = 0.008$) [Fig. 3(f)]. In contrast, the AuNC@BSA, which did not include Gd modification and served as the control group, was unable to provide contrast in the cartilage image.

After 24 h of incubation of cartilage plugs with AuNC@BSA-Gd-I, higher attenuation was observed in defective cartilage compared to healthy plugs. Additionally, increased attenuation was noted in damaged cartilage with a 90 kVp tube voltage compared to 60 kVp [Fig. 3(g)]; however, the increase did not improve the correlation with sGAG content ($R^2 = 0.83$, $P = 0.0017$ at 60 kVp; $R^2 = 0.75$, $P = 0.0053$ at 90 kVp) [Fig. 3(h)]. Normalization of the results did not yield a comparable effect to unnormalized results ($R^2 = 0.77$, $P = 0.004$ at 60 kVp, $R^2 = 0.72$, $P = 0.008$ at 90 kVp) (Fig. S4), but it still provided a valuable method for assessing cartilage health.

D. Imaging potential and cartilage visualization of AuNC@BSA-Gd-I for optical imaging

The IVIS (In Vivo Imaging System) with different field of view (FOV) settings was used to assess the fluorescence imaging capabilities of AuNC@BSA-Gd-I. Dosages ranging from 2.5 mg/ml (0.072 mg Au/ml) to 20 mg/ml (0.358 mg Au/ml) of AuNC@BSA-Gd-I were imaged and subjected to quantitative analysis. The AuNC@BSA-Gd-I emitted fluorescence was clearly detected at each concentration [Figs. 4(a) and 4(c)]. Due to the rapid scanning capability of IVIS, imaging was performed at different time points (0, 1, 4, 8, 12, and 24 h) after the incubation of cartilage plugs with AuNC@BSA-Gd-I. The results showed that AuNC@BSA-Gd-I gradually accumulated in OA-mimicking cartilage starting at 1 h and reached its peak at 12 h post-incubation, followed by a washout of AuNC@BSA-Gd-I. In contrast, the healthy plugs exhibited slower absorption of AuNC@BSA-Gd-I, with washout not occurring within 24 h post-incubation [Figs. 4(b), 4(d), and S5(a)]. The DMMB results demonstrated an inverse correlation of fluorescent intensity at 24 h post-incubation with sGAG content in cartilage (unnormalized results: $R^2 = 0.79$, $P = 0.003$, normalized results: $R^2 = 0.81$, $P = 0.002$) [Figs. 4(e) and S5(b)]. Apart from 24 h, the fluorescence acquired at each time point established a correlation with

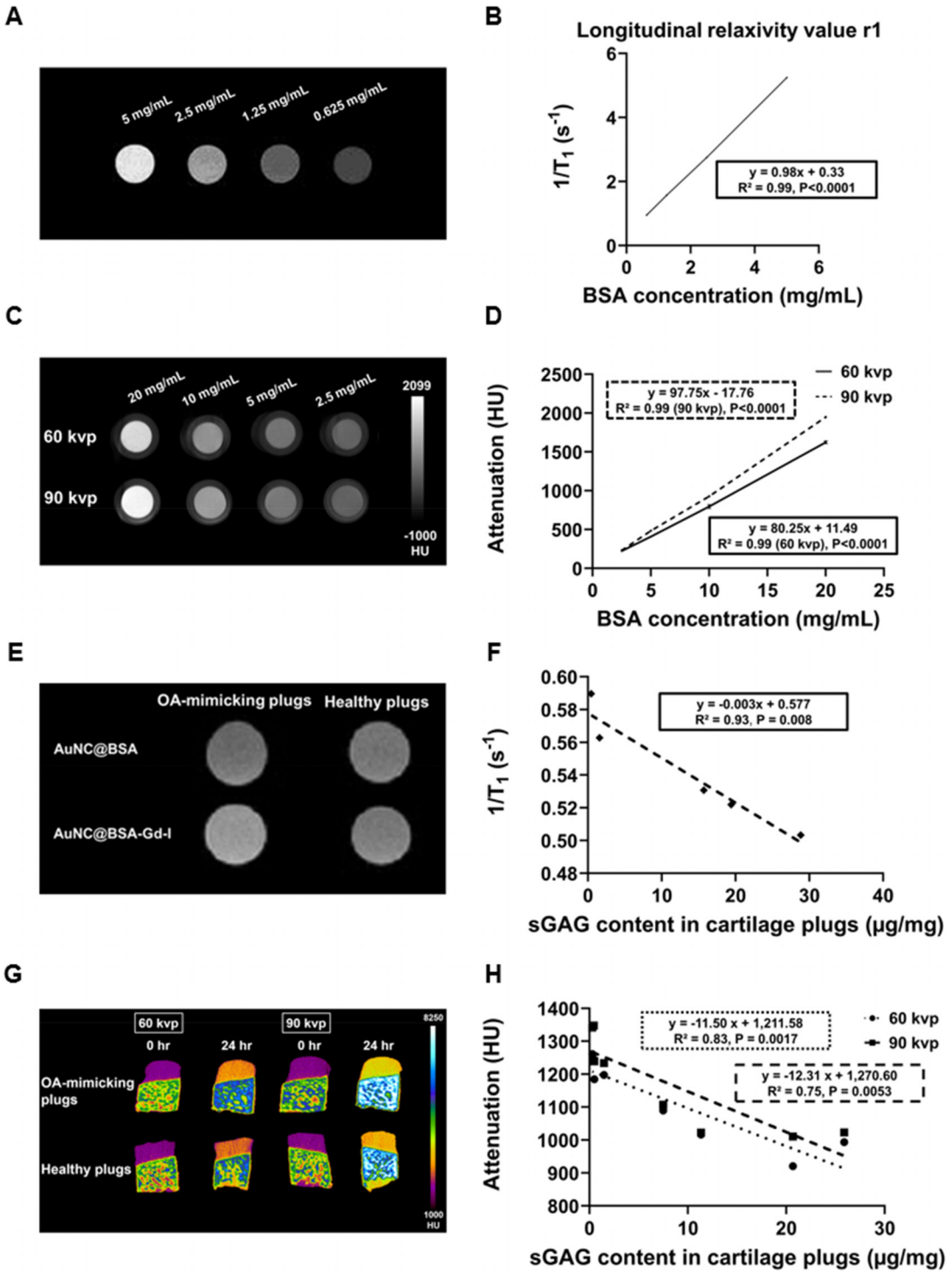

FIG. 3. MRI and CT imaging potential of AuNC@BSA-Gd-I for cartilage. (a) T1-weighted imaging was performed using AuNC@BSA-Gd-I, and (b) quantitative analysis was conducted at concentrations ranging from 0.625 to 5 mg/ml. (c) CT imaging of AuNC@BSA-Gd-I was conducted using 60 or 90 kVp, with concentrations ranging from 2.5 to 20 mg/ml. (d) Hounsfield Unit (HU) values for each concentration were recorded. (e) Cartilage tissue in papain solution was subjected to quantitative analysis at 9.4 T MRI 24 h post-incubation with AuNC@BSA-Gd-I. (f) Correlation of T1 relaxivity with sGAG content in cartilage. (g) CT imaging and analysis of cartilage plugs were performed at 60 or 90 kVp before and after 24 h of incubation with AuNC@BSA-Gd-I. (h) Correlation of attenuation in cartilage regions at 60 or 90 kVp with sGAG content in cartilage.

sGAG content. Notably, the R-squared value has been higher than 0.7 since 8 h post-incubation in both unnormalized and normalized results [Figs. S5(c) and S5(d)]. The calculation of fluorescent intensity in the surrounding medium could provide additional information to assess the cartilage condition. Therefore, the solution incubated with cartilage plugs was also analyzed by IVIS. The signal generated from the solution generally decreased in both healthy and defective cartilage, with the decrease being faster in defective cartilage compared to healthy cartilage [Fig. S5(e)]. The value obtained by dividing the fluorescent intensity in cartilage by that in the solution showed that AuNC@BSA-Gd-I continuously accumulated in cartilage over time in both healthy and damaged cartilage [Fig. S5(f)]. However, the uptake ratio revealed that the peak uptake occurred at 12 h after incubation in damaged cartilage [Fig. S5(g)], which is similar to the results gathered from quantitative fluorescent intensity [Fig. 4(d)]. It might be attributed to the absorption of AuNC@BSA-Gd-I in the bone portion of the plugs affecting the uptake ratio in cartilage. However, including the bone portion is necessary to highlight the interface between cartilage and bone during visualization. Finally, the correlation of fluorescent intensity collected from the medium at each time point with sGAG was recorded [Fig. S5 (h)].

E. Synthesis of AuNC@BSA-Gd-^{131}I and its potential for damaged cartilage detection

Chloramine-T is one of the oxidizing agents widely used for iodination or radioiodination via conjugation with tyrosine residues.[32,33] Herein, we have adopted the method to synthesize AuNC@BSA-Gd-I, and we further tested it for the synthesis of AuNC@BSA-Gd-^{131}I. The purified AuNC@BSA-Gd-^{131}I exhibited a high radiochemical purity (approximate 100%) with a 16.6 ± 9.8% yield [Figs. 5(a) and 5(b)]. Next, OA-mimicking (N = 3) and healthy cartilage (N = 3) plugs were soaked in purified AuNC@BSA-Gd-^{131}I for 24 h, and the results were statistically tested using a Welch's t-test or pooled t-test. Although AuNC@BSA-Gd-^{131}I did not significantly accumulate in damaged cartilage compared to healthy cartilage (23 755.38 ± 5993.61 CPM/mg vs 11 699.97 ± 794.93 CPM/mg, P = 0.071, Power = 0.73) [Fig. 5(c)], the normalized results of AuNC@BSA-Gd-^{131}I in OA-mimicking plugs were significantly higher than in healthy cartilage plugs (68.21 ± 4.44% vs 51.06 ± 3.69%, P = 0.007, Power = 0.96) [Fig. 5(d)]. The normalization considered the percentage of cartilage uptake in the whole plugs, which minimized the effect of absorption in the bone portion, thus providing a more realistic uptake in the *in vitro* model. Of note, we have demonstrated the preliminary feasibility of synthesizing AuNC@BSA-Gd-^{131}I using radioiodine, thereby expanding the application of the AuNC@BSA-Gd-I, providing an effective strategy for assessing defective cartilage.

F. Assessment of cartilage defects in porcine plugs using current gold nanomaterials

Iodine (I), gold (Au), bismuth (Bi), barium (Ba), and lanthanides (Ln) are widely used to develop contrast agents for CT scanning.[34] T1-weighted MRI contrast agents generally contain gadolinium (Gd), manganese (Mn), or ferric (Fe^{3+}) cations.[35] Any of the elements mentioned earlier can potentially be modified onto AuNC@BSA to apply for fluorescent imaging, CT imaging, and MR imaging. Consequently, we tested the imaging potential of current ionic nanomaterials, including those utilizing similar elements to AuNC@BSA-Gd-I for synthesis. These include basic AuNC@BSA,[18] AuNC@BSA-I,[36] and AuNC@BSA-Gd,[37] and the cationic nanomaterial AuNC@CBSA.[38] Due to their small size and ionic properties, these gold nanomaterials have the potential to serve as a multimodal probe for cartilage visualization. Furthermore, given that Gd has been reported to provide

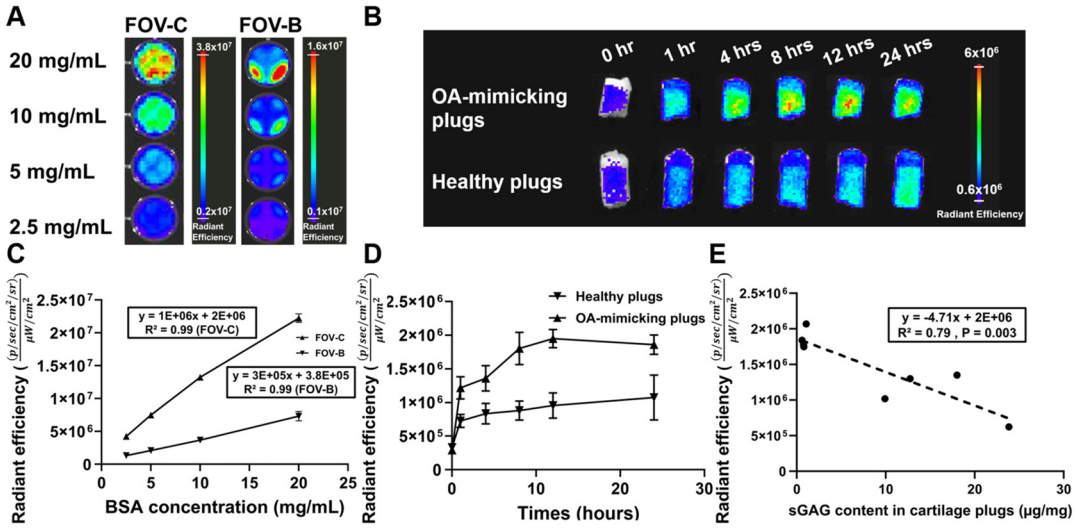

FIG. 4. Exploration of optical imaging potential for cartilage tissue using AuNC@BSA-Gd-I nanomaterial. (a) Fluorescent images of AuNC@BSA-Gd-I were detected by the IVIS system at concentrations ranging from 2.5 to 20 mg/ml in FOV-C (12.9 cm) or FOV-B (6.5 cm). (b) Fluorescent signals of the cartilage plugs were acquired at 0 (before), 1, 4, 8, 12, and 24 h after incubation with AuNC@BSA-Gd-I. (c) Quantitative imaging analysis of AuNC@BSA-Gd-I at concentrations from 2.5 to 20 mg/ml. (d) Imaging intensity comparison of healthy and OA-mimicking cartilage at different time points following AuNC@BSA-Gd-I accumulation. (e) Establishment of a correlation between the sGAG content in cartilage and fluorescent intensity measured at 24 h.

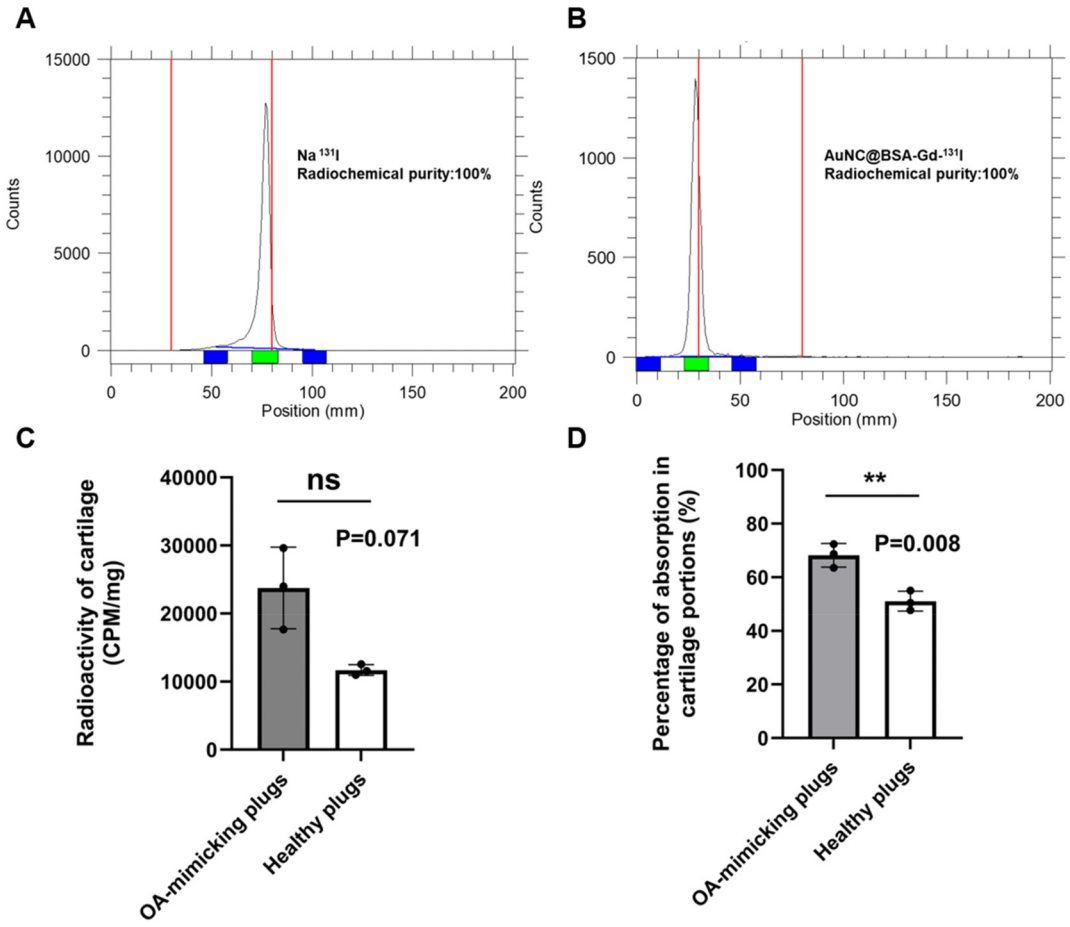

FIG. 5. The synthesis of AuNC@BSA-Gd-^{131}I and its potential for assessing damaged cartilage were examined. (a) The radiochemical purity of sodium iodide (^{131}I) and (b) AuNC@BSA-Gd-^{131}I was analyzed using RP-TLC on a silica-gel-impregnated paraffin oil plate. (c) Calculating the radioactivity in both defective cartilage (N = 3) and healthy cartilage (N = 3). (d) Comparing the percentage of radioactivity within the cartilage portion of the entire plug between damaged (N = 3) and healthy cartilage (N = 3). Statistical differences in (c) were assessed using Welch's t-test, and in (d) using the pooled t-test. Data are presented as mean ± SD (**$p < 0.01$) or not significant (ns).

contrast enhancement for CT and MRI,[39] AuNC@BSA-Gd may be a promising gold nanomaterial for multimodal imaging without the need for iodine modification. Thus, we compared the imaging ability and versatility of current candidate nanomaterials with AuNC@BSA-Gd-I. Initially, we supplemented additional details regarding the physicochemical characteristics of those current candidates. The absorption and excitation/emission profiles were similar in each candidate, except for AuNC@BSA-I, which exhibited a peak absorption at approximately 225 nm due to the presence of I^- [Figs. S6(a)–S6(d)]. All candidates emitted red fluorescence under 365 nm UV light [Figs. S6(e) and S6(f)]. The exact size, hydrodynamic radius, and zeta potentials of the candidates were measured by TEM or DLS analyzer, and the outcomes demonstrated that the candidates have a small size (<20 nm) with ionic properties, which may be appropriate for cartilage imaging [Figs. S6(g)–S6(i)]. The alteration in zeta potential for AuNC@BSA-I and AuNC@BSA-Gd-I, compared to that of AuNC@BSA and AuNC@BSA-Gd, respectively, demonstrated the surface modifications. Next, the cytotoxicity of the candidates and AuNC@BSA-Gd-I was assessed. Although these nanomaterials did not cause obvious damage to mouse chondrocytes at 12 h post-treatment, the cell viability of chondrocytes decreased to 78.5 ± 0.03% and 75.66 ± 3.55% at 24 h in the 20 mg/ml concentration groups treated with AuNC@BSA-I and AuNC@BSA-Gd, respectively (Fig. S7). In addition, the characteristics of AuNC@CBSA were examined and verified to be cationic [Figs. S8(a)–S8(d)], potentially allowing positive accumulation in cartilage tissue.

Due to the presence of Gd, AuNC@BSA-Gd is the only candidate capable of enhancing contrast in T1-weighted MR imaging. The images and quantitative analysis demonstrated that concentrations as low as 0.625 mg/ml of AuNC@BSA-Gd (0.0149 mg Gd/ml) could be visualized, and the r1 value was 0.86 s^{-1} per mg/ml [Figs. 6(a) and 6(b)]. For CT imaging and analysis, AuNC@BSA-I (20 mg/ml, 0.705 mg I/ml), which was modified with iodine, exhibited the highest HU value among all candidates. In contrast, AuNC@BSA and AuNC@BSA-Gd showed only slight enhancement at both 60 and 90 kVp outputs [Figs. 6(c) and 6(d) and Figs. S9(a)–S9(d)]. Additionally, at each concentration, AuNC@BSA-I exhibited significantly higher attenuation at both 60 and 90 kVp compared to AuNC@BSA and

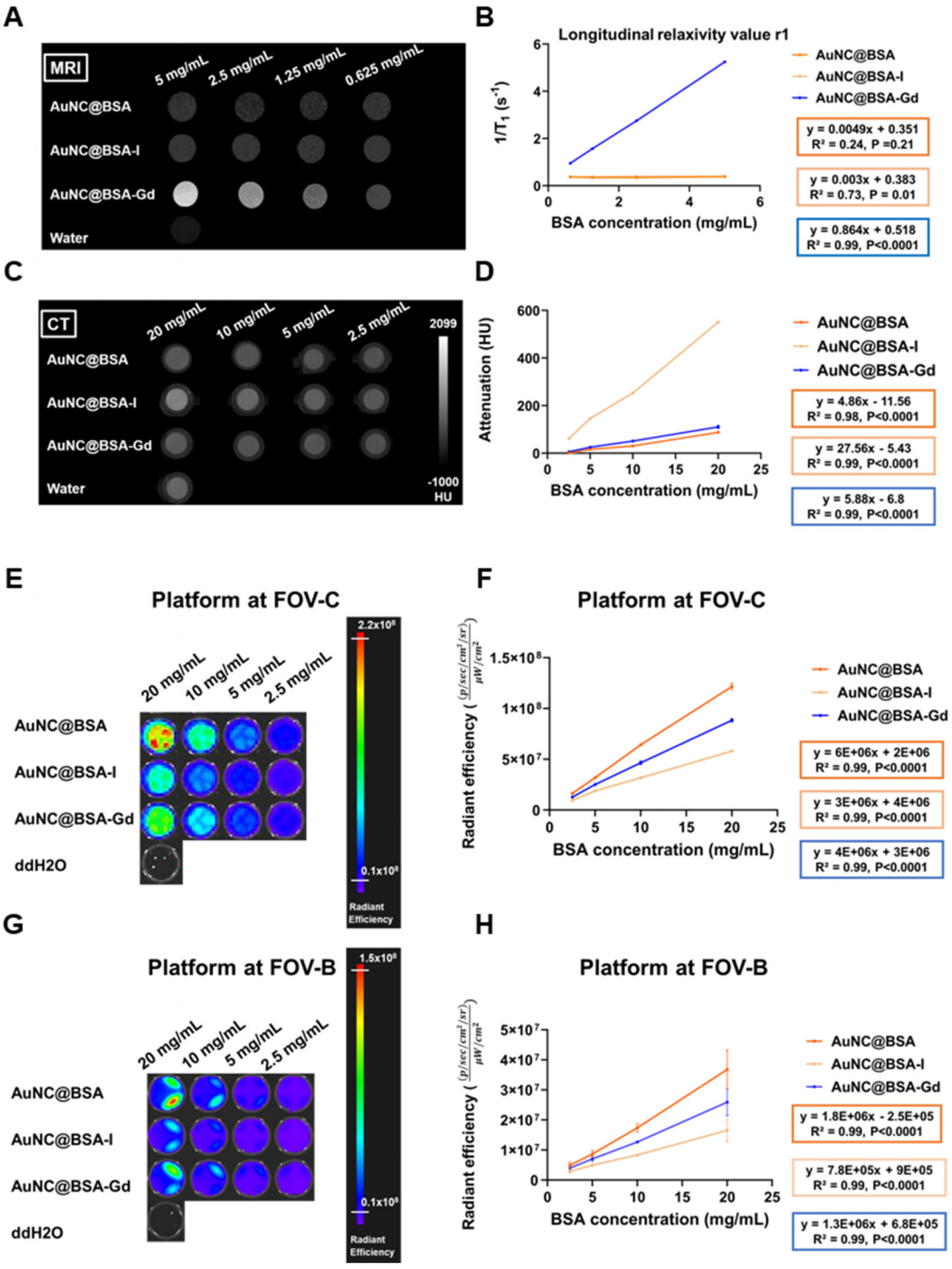

FIG. 6. Imaging potentials of candidate nanomaterials. (a) The imaging potential of nanomaterials for MRI and their (b) quantitative results. The individual slopes correspond to the longitudinal relaxivity value (r1). (c) The assessment of CT imaging capabilities exhibited by nanomaterials ranging from 2.5 to 20 mg/ml. (d) Quantitative analysis of CT images. (e) The optical images of nanomaterials were acquired by IVIS, encompassing concentrations from 2.5 to 20 mg/ml. (f) The quantitative results of nanomaterials at FOV-C. (g) Images and (h) quantitative analysis of selected nanomaterials acquired at FOV-B. Orange line, AuNC@BSA; pearl line, AuNC@BSA-I; blue line, AuNC@BSA-Gd. FOV-C, 12.9 cm; FOV-B, 6.5 cm.

AuNC@BSA-Gd (Table S1). The insufficient enhancement might be attributed to the higher k-edge values of Au (80.1 keV) and Gd (50.2 keV). The upper limitation of our system was 90 kVp; however, gold is reported to exhibit obvious attenuation of x rays only at potentials higher than 120 kVp.[40] Additionally, the energy received by the object would be affected by the system's efficiency. Regarding fluorescence imaging, at the FOV-C position, AuNC@BSA exhibited the highest signal among all candidates, followed by AuNC@BSA-Gd and AuNC@BSA-I. However, this significance was only observed at 10 and 20 mg/ml concentrations at the FOV-B position, suggesting that the FOV-C position is more suitable for *in vitro* model examination [Figs. 6(e)–6(h) and Table S2]. The lower fluorescent intensity observed in both AuNC@BSA-I and AuNC@BSA-Gd-I might be caused by the introduction of NaI (Fig. S10). Although iodide did not impact the fluorescent emission of AuNC@BSA, iodine (I_2) could be released from iodide by the oxidizing agent chloramine-T. Subsequently, the excess iodide reacted with iodine, resulting in the etching of the gold.[41,42]

The cartilage containing candidates was subjected to three types of imaging modalities, previously utilized for AuNC@BSA-Gd-I. In MRI, AuNC@BSA-Gd showed enhancement in T1-weighted images, penetrating the cartilage and increasing the contrast of the cartilage tissue [Fig. 7(a) and Table S3]. For CT imaging and quantitative analysis, AuNC@BSA-I significantly ($P < 0.0001$) exhibited higher contrast in defective cartilage (325.51 ± 12.97 HU) compared to healthy cartilage (161.51 ± 15.2 HU) at 60 kVp output. The normalized imaging results further indicated that defective cartilage (5.74 ± 0.21) exhibited significantly ($P = 0.02$) higher fold changes compared to the control group (1.50 ± 0.14) after incubation with AuNC@BSA-I [Fig. 7(b) and Table S4]. However, this significant difference was not observed in other candidates. Unexpectedly, when compared to OA-mimicking plugs, the cationic AuNC@CBSA did not exhibit a tendency to accumulate in healthy plugs, defying our initial assumptions, despite the insufficient signal generated [Fig. 7(b) and Table S4]. Regarding IVIS analysis for candidate nanomaterials, the quantitative analysis and normalized results demonstrated that variations gradually occurred from 3 h post-incubation [Figs. 7(c) and 7(d) and Figs. S11(a)–S11(d)].

The correlation, whether positive or inverse, between 24-h imaging intensity and sGAG content was verified. Interestingly, the correlation obtained from AuNC@BSA and AuNC@CBSA, which were not modified with other imaging materials such as iodine or gadolinium, showed a better R-squared value [Figs. 7(e)–7(h)]. While the imaging intensity generated from some candidates was not significantly correlated with sGAG content in cartilage, this might be attributed to the limited sample size. Nevertheless, the non-normalized and normalized results of imaging intensity obtained from AuNC@BSA, AuNC@BSA-Gd, and AuNC@CBSA significantly distinguished damaged cartilage from healthy cartilage, suggesting that these candidates have potential for cartilage imaging using IVIS (Table S5). Although AuNC@BSA performs better than the nanomaterial we developed for optical *in vitro* imaging, optical signals face significant challenges in translating to clinical use due to current penetration limitations. Nonetheless, the rapid scanning and outstanding sensitivity of optical imaging allow it to excel in *in vitro* verification and *in vivo* small animal studies. Our results also indicated that AuNC@BSA-Gd-I remains a valuable tool for *in vitro* fluorescent analysis despite its weaker fluorescence. Therefore, increasing the fluorescent intensity to be comparable to AuNC@BSA may not be our primary focus. Collectively, the candidates excel in unimodal or multimodal imaging abilities for cartilage, whereas their multimodal potential is not comparable to AuNC@BSA-Gd-I.

In terms of the limitations of this study, although the candidates selected were not as versatile as AuNC@BSA-Gd-I, our choices were limited to materials exhibiting similar characteristics that had been previously investigated. For example, the cationic AuNC@BSA-Gd-I should be further developed and tested for its multimodal imaging potential in cartilage. Given that the absence of iodine labeling resulted in insufficient x-ray attenuation in our CT system, the imaging potential of cationic AuNC@CBSA may not be directly comparable to that of anionic AuNC@BSA-Gd-I.

III. CONCLUSIONS

Our findings demonstrated that while current gold nanomaterials exceled in imaging capabilities for cartilage, their utility is limited to unimodal or dual-modal imaging. In contrast, the AuNC@BSA-Gd-I exhibited multifunctional applications across different biomedical instruments for detecting defective cartilage. Additionally, the probe can potentially be further modified with therapeutic molecules to develop a multimodal theranostic strategy for cartilage defects. Collectively, the probe not only offers a versatile solution for medical institutes and research centers but also provides a more effective, visible, and convenient assessment of cartilage defects.

IV. METHODS

A. Synthesis of AuNC@BSA-Gd-I

The AuNC@BSA-Gd was synthesized by incubating gadolinium chloride (0.15 ml, 500 mM) with an $HAuCl_4$ solution (5 ml, 10 mM) under vigorous stirring at 37 °C, followed by the addition of a BSA solution (50 mg/ml). After 10 min, 0.75 ml of NaOH (1 M) was added, and the mixture was incubated for at least 12 h at 200 rpm.[37] The mixture was then filtered using a 0.22 μm syringe filter and further purified with Amicon® Ultra-15 centrifugal filters (30 kDa MWCO) to eliminate smaller molecules and concentrate the solution. The purified AuNC@BSA-Gd (0.44 ml) was mixed with 0.2 ml of NaI (5 M) and 0.2 ml of chloramine-T (1.25 mg/ml) at room temperature with agitation at 200 rpm for 20 min. The solution was subsequently purified by dialysis and filtration.

B. Establishment of an *in vitro* OA-mimicking model using porcine

Fresh porcine knees were sourced from a local slaughterhouse that supplies meat production in Kaohsiung, Taiwan. The cartilage plugs were extracted using a 3-mm diameter hollow punch. After extraction, the plugs were washed three times with PBS and then stored at −20 °C [Fig. S3(a)].[28] To prepare plugs mimicking osteoarthritis (OA), they were incubated with 0.25% Trypsin-EDTA for 12 h at 37 °C with gentle shaking. To assess the effectiveness of the procedure, the homogeneity of sGAG content degradation was evaluated by subjecting the OA-mimicking plugs to safranin O staining ($N = 4$), while healthy plugs immersed in PBS served as controls ($N = 4$). In subsequent imaging examinations, the solution containing nanomaterials was adjusted to a final concentration of 7.5% glucose to approximate the osmolality of articular cartilage, which typically falls within the range of 350–450 mOsm/kg.[43] The plugs immersed in a 7.5% glucose solution were used as the control group.

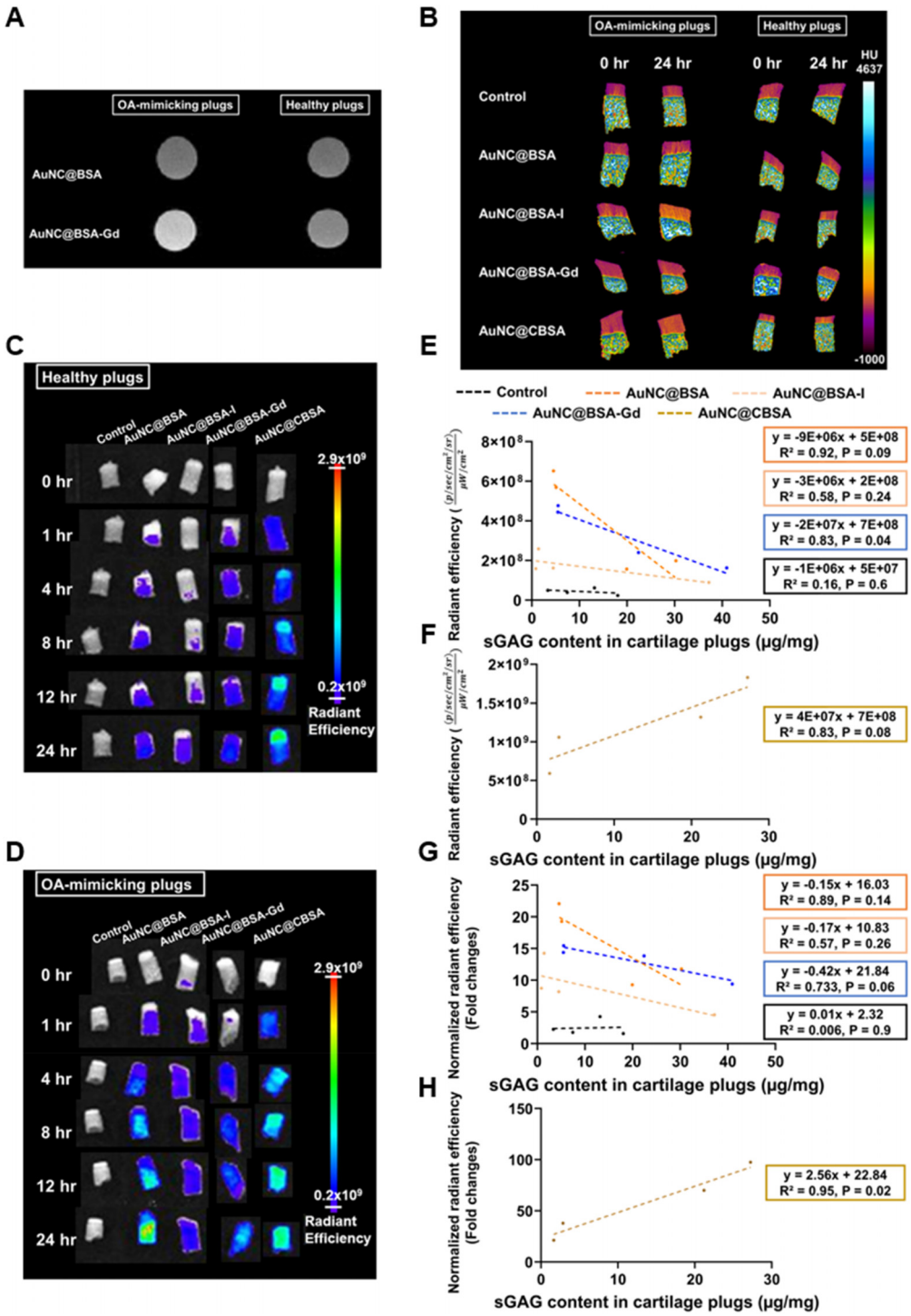

FIG. 7. Cartilage imaging capabilities of the candidate nanomaterials for MRI, CT, and IVIS. (a) Cartilage specimens were incubated with AuNC@BSA (control) and AuNC@BSA-Gd for 24 h, followed by dissolution using a papain reagent to perform MRI image acquisition. (b) The tissue plugs were immersed in the candidate nanomaterials and imaged by μCT at before and 24 h after treatment. (c) Images were acquired by IVIS at various time points (0, 1, 4, 8, 12, and 24 h) after the incubation of candidate nanomaterials with OA-mimicking plugs or (d) healthy plugs. The correlation between the quantitative imaging analysis and normalized imaging results with the sGAG content at 24 h post-incubation is examined for both (e) and (f) anionic materials and (g) and (h) cationic AuNC@CBSA. Solid line, healthy plugs; dotted line, OA-mimicking plugs; orange line, AuNC@BSA; pearl line, AuNC@BSA-I; blue line, AuNC@BSA-Gd; black line, control; brown line, AuNC@CBSA.

C. MRI acquisition and analysis

T1-weighted MR images of gold nanomaterials were obtained using a 9.4 T animal MRI system (Biospec 94/20, Bruker, Massachusetts, United States). The nanomaterials were immobilized by adding an equal volume of 2% agar to the solution before the MRI scan. The T1 relaxation time (ms) was determined for gold nanomaterials within the concentration range of 0.625–5 mg/ml (N = 3 at each concentration) using T1-weighted pulse sequences. The measurement parameters were as follows: T1-weighted sequence, spin echo (SE), the repetition time (TR) = 300 ms, echo Time (TE) = 5 ms, slice thickness = 2 mm, and slice gap = 0.38 mm. To determine signal intensities, the relaxivity values of r1 were calculated by correlating the 1/T1 relaxation time (s^{-1}) with BSA concentration (mg/ml) curves.

To analyze the content of nanomaterials in OA-mimicking cartilage (N = 3) and healthy cartilage (N = 3), the cartilage was removed from the plugs using a disposable microtome blade, which was discarded once it became blunt to prevent tearing of the cartilage. After a 24-h incubation with 5 mg/ml nanomaterials, a papain solution was used to dissolve the cartilage. Once complete dissolution was achieved, the samples were fixed for MRI acquisition and analysis. The quantitative results were presented in 1/T1 relaxation time (s^{-1}) or as normalized results (Fold changes, OA-mimicking plugs/healthy plugs).

D. CT visualization and analysis

The imaging potential of each gold nanomaterial (2.5, 5, 10, and 20 mg/ml, N = 3) was evaluated using micro-CT (Skyscan 1176, Bruker, Massachusetts, United States). The parameter settings were as follows: tube potentials, 60 kVp (N = 3 at each concentration) or 90 kVp (N = 3 at each concentration); tube current, 100 μA; exposure, 1500 ms; filter = Al 0.5 mm. Images of OA-mimicking cartilage and healthy cartilage were initially acquired before immersing each nanomaterial (20 mg/ml, N = 4). After 24 h, each plug was imaged again to collect images of cartilage containing the nanomaterials. Several adjustments were applied before reconstruction, including beam-hardening correction = 20, ring-artifacts reduction = 12, and smoothing = 5. To calibrate the quantitative results, water was imaged, and its Hounsfield unit was set as zero before reconstruction. Once the reconstruction was completed, regions of interest (ROIs) were extracted and analyzed in the cartilage region or centers of solution using CT Analyzer software. The normalized results were calculated by taking the attenuation obtained at 24 h and dividing it by the attenuation at the zero-time point. The images of gold nanomaterials were presented in volume view using CTvox software. To observe the images more clearly, both grayscale and color scale images were provided.

E. IVIS imaging and analysis

The fluorescent imaging potential of nanomaterials was assessed using IVIS (PerkinElmer, Waltham, MA, USA). The parameters are configured as follows: F/Stop = 2, Binning = 8, and Exposure = auto. For nanomaterials, the field of view (FOV) is set to C (12.9 cm) or B (6.5 cm). For plugs, the FOV is set to B. Concentrations ranging from 5 to 20 mg/ml were tested (N = 3). The OA-mimicking plugs or healthy plugs containing nanomaterials (5 mg/ml) were imaged at various timepoints, including 0, 1, 4, 8, 12, and 24 h (N = 4, AuNC@BSA-Gd-I; N = 3, each candidate). The timepoint labeled as "0" represented the plugs before they were soaked into the solution containing nanomaterials. Regions of interest (ROIs) were extracted from the cartilage regions, and quantitative results were calculated. The average imaging intensity results were presented as radiant efficiency, and the normalized results were determined by calculating the average radiant efficiency in cartilage acquired at each time point divided by the average radiant efficiency in cartilage acquired at the zero-time point. The average imaging intensity in the medium was measured concurrently with cartilage at each time point. The average radiant efficiency in cartilage at each time point was divided by that in the medium. The uptake ratio was estimated using the following formula:

$$\text{Uptake ratio}\,(\%) = \left(\frac{\text{Average radiant efficiency in cartilage at each time points} - \text{Average radiant efficiency in cartilage at 0 h}}{\text{Average radiant efficiency in medium at 0 h}}\right) \times 100\%.$$

SUPPLEMENTARY MATERIAL

See the supplementary material for additional methods, including the examination of materials' physical and chemical properties, DMMB assay, and the synthesis of candidate nanomaterials. Supplementary figures and tables regarding the verification of sGAG degradation by Safranin O staining, the characterization of candidate nanomaterials, and normalized results of each imaging intensity for the nanomaterials were provided.

ACKNOWLEDGMENTS

We acknowledge the Institute of Nuclear Energy Research (INER) for kindly providing $Na^{131}I$. We also acknowledge the Department of Materials and Optoelectronic Science, National Sun Yat-sen University, Kaohsiung, Taiwan, for technical support in TEM imaging. We acknowledge the Core Facility Center, National Cheng Kung University, Tainan, Taiwan, for their assistance in conducting the ICP-MS analysis. We extend our gratitude to the Center for Laboratory Animals, Core Laboratory for Gnotobiotic Biomedicine, and the Molecular Imaging Core of the Institute for Translational Research in Biomedicine at Kaohsiung Chang Gung Memorial Hospital, Kaohsiung, Taiwan, for their technical and facility support related to IVIS Spectrum, 9.4T animal MRI, and the establishment of the disease model. We also acknowledge the Taiwan Animal Consortium for the use of facilities. We thank Dr. Yi-An Chen (Institute of Biological Chemistry, Academia Sinica, Taiwan) for her constructive criticism and personal insight.

This work was financially supported by the National Health Research Institute, Taiwan (No. NHRI-EX113-11029SI), the National Science and Technology Council (No. NSTC 112-2314-B-182A-105-MY3), and the Chang Gung Memorial Hospital, Taiwan (Nos. CMRPG8N0781 and CMRPG8M1281-3).

AUTHOR DECLARATIONS

Conflict of Interest

The authors have no conflicts to disclose.

Ethics Approval

Ethics approval for experiments reported in this title on animal or human subjects was granted. The experiment investigating the toxicity of nanomaterials on mouse chondrocytes was approved by the Institutional Animal Care and Use Committee (IACUC No. 2022122304) at the Chang Gung Memorial Hospital Laboratory Animal Center.

Author Contributions

Cheng-Hsiu Lu and Wei-Shiung Lian contributed equally to this work.

Cheng-Hsiu Lu: Conceptualization (equal); Methodology (equal); Project administration (supporting); Writing – original draft (lead). **Wei-Shiung Lian:** Conceptualization (equal); Data curation (equal); Funding acquisition (lead); Supervision (supporting). **Re-Wen Wu:** Resources (lead); Validation (equal); Visualization (supporting). **Yu-Han Lin:** Formal analysis (lead); Investigation (equal). **Chia−Hao Su:** Investigation (equal); Methodology (equal). **Chuan-Lin Chen:** Software (lead); Visualization (equal). **Ming-Hong Tai:** Project administration (lead); Resources (supporting). **Yu-Shan Chen:** Data curation (equal); Software (supporting). **Shao-Yu Wang:** Project administration (supporting); Validation (equal). **Chao-Cheng Chen:** Software (supporting); Validation (supporting). **Feng-Sheng Wang:** Supervision (lead); Visualization (equal); Writing – review & editing (lead).

DATA AVAILABILITY

The data that support the findings of this study are available within the article and its supplementary material.

REFERENCES

[1]A. J. Sophia Fox, A. Bedi, and S. A. Rodeo, Sports Health **1**, 461–468 (2009).
[2]X. Gao, A. N. Patwa, Z. Deng, H. Utsunomiya, M. W. Grinstaff, J. J. Ruzbarsky, B. D. Snyder, S. Ravuri, M. J. Philippon, and J. Huard, Am. J. Transl. Res. **13**, 8921–8937 (2021).
[3]R. C. Stewart, P. N. Bansal, V. Entezari, H. Lusic, R. M. Nazarian, B. D. Snyder, and M. W. Grinstaff, Radiology **266**, 141–150 (2013).
[4]S. Fantoni, I. Gabucci, P. Cardarelli, G. Paterno, A. Taibi, V. Cristofori, C. Trapella, A. Bazzani, M. Assenza, A. Zanna Bonacorsi, D. Conti, and F. Baruffaldi, Diagnostics **12**, 2111 (2022).
[5]J. Casale and J. S. Crane, in *StatPearls* (StatPearls Publishing, Treasure Island, FL, 2021), https://pubmed.ncbi.nlm.nih.gov/31335015/.
[6]A. M. Bhosale and J. B. Richardson, Br. Med. Bull. **87**, 77–95 (2008).
[7]X. Li, B. Dai, J. Guo, L. Zheng, Q. Guo, J. Peng, J. Xu, and L. Qin, Nanomicro Lett. **13**, 149 (2021).
[8]J. D. Freedman, H. Lusic, B. D. Snyder, and M. W. Grinstaff, Angew. Chem., Int. Ed. Engl. **53**, 8406–8410 (2014).
[9]S. Xiao, Y. Tang, Y. Lin, Z. Lv, and L. Chen, Acta Biomater. **109**, 153–162 (2020).
[10]T. Lawson, A. Joenathan, A. Patwa, B. D. Snyder, and M. W. Grinstaff, ACS Nano **15**, 19175–19184 (2021).
[11]C. Zhang, A. Vedadghavami, T. He, J. F. Charles, and A. G. Bajpayee, ACS Nano **17**, 6649–6663 (2023).
[12]S. Thangudu, C. C. Yu, C. L. Lee, M. C. Liao, and C. H. Su, J. Nanobiotechnol. **20**, 157 (2022).
[13]G. Antoch and A. Bockisch, Eur. J. Nucl. Med. Mol. Imaging **36**, 113–120 (2009).
[14]J. Cheon and J. H. Lee, Acc. Chem. Res. **41**, 1630–1640 (2008).
[15]R. A. Leitgeb and B. Baumann, Front. Phys. **6**, 114 (2018).
[16]M. Wu and J. Shu, Contrast Media Mol. Imaging **2018**, 1382183.
[17]B. Wu, S. T. Lu, H. Yu, R. F. Liao, H. Li, B. V. Lucie Zafitatsimo, Y. S. Li, Y. Zhang, X. L. Zhu, H. G. Liu, H. B. Xu, S. W. Huang, and Z. Cheng, Biomaterials **159**, 37–47 (2018).
[18]J. Xie, Y. Zheng, and J. Y. Ying, J. Am. Chem. Soc. **131**, 888–889 (2009).
[19]I. Fabijanic, M. Jurkovic, D. Jaksic, and I. Piantanida, Materials **15**, 8448 (2022).
[20]Y. Zheng, J. Wu, H. Jiang, and X. Wang, Coord. Chem. Rev. **431**, 213689 (2021).
[21]L. Chen, M. Gharib, Y. Zeng, S. Roy, C. K. Nandi, and I. Chakraborty, Mater. Today Chem. **29**, 101460 (2023).
[22]C. Zhang, X. Gao, W. Chen, M. He, Y. Yu, G. Gao, and T. Sun, iScience **25**, 105022 (2022).
[23]X. Y. Wong, D. Quesada-Gonzalez, S. Manickam, S. Y. New, K. Muthoosamy, and A. Merkoci, Sci. Rep. **11**, 2375 (2021).
[24]M. Wu, Y. Zhang, N. Zhuo, M. Wu, Z. Ye, and X. Zhang, Int. J. Nanomed. **15**, 227–238 (2020).
[25]M. Kim and J.-W. Yeon, J. Radioanal. Nucl. Chem. **330**, 469–473 (2021).
[26]J. P. Schlomka, E. Roessl, R. Dorscheid, S. Dill, G. Martens, T. Istel, C. Baumer, C. Herrmann, R. Steadman, G. Zeitler, A. Livne, and R. Proksa, Phys. Med. Biol. **53**, 4031–4047 (2008).
[27]J. T. Bushberg, *The Essential Physics of Medical Imaging*, 3rd ed. (Wolters Kluwer Health/Lippincott Williams & Wilkins, Philadelphia, 2012).
[28]P. Bowland, R. M. Cowie, E. Ingham, J. Fisher, and L. M. Jennings, Proc. Inst. Mech. Eng., Part H **234**, 163–170 (2020).
[29]J. Zhang, L. Xiao, L. Tong, C. Wan, and Z. Hao, Ultrasound Med. Biol. **44**, 861–871 (2018).
[30]M. K. M. Honkanen, A. E. A. Saukko, M. J. Turunen, W. Xu, G. Lovric, J. T. J. Honkanen, M. W. Grinstaff, V. P. Lehto, and J. Toyras, Ann. Biomed. Eng. **48**, 556–567 (2020).
[31]F. Dengu, F. Neri, E. Ogbemudia, G. Ebeling, L. Knijff, K. Rozenberg, R. Dumbill, J. Branchereau, P. Friend, R. Ploeg, and J. Hunter, Ann. Transl. Med. **10**, 1 (2022).
[32]S. C. Tzou, S. Roffler, K. H. Chuang, H. P. Yeh, C. H. Kao, Y. C. Su, C. M. Cheng, W. L. Tseng, J. Shiea, I. H. Harm, K. W. Cheng, B. M. Chen, J. J. Hwang, T. L. Cheng, and H. E. Wang, Radiology **252**, 754–762 (2009).
[33]M. N. Chao, J. M. Chezal, E. Debiton, D. Canitrot, T. Witkowski, S. Levesque, F. Degoul, S. Tarrit, B. Wenzel, E. Miot-Noirault, A. Serre, and A. Maisonial-Besset, Pharmaceuticals **15**, 162 (2022).
[34]Z. Jiang, M. Zhang, P. Li, Y. Wang, and Q. Fu, Theranostics **13**, 483–509 (2023).
[35]C. Geraldes, Molecules **29**, 1352 (2024).
[36]X. Chen, H. Zhu, X. Huang, P. Wang, F. Zhang, W. Li, G. Chen, and B. Chen, Nanoscale **9**, 2219–2231 (2017).
[37]W. Le, S. Cui, X. Chen, H. Zhu, B. Chen, and Z. Cui, Nanomaterials **6**, 65 (2016).
[38]R. Liu, W. Xiao, C. Hu, R. Xie, and H. Gao, J. Control Release **278**, 127–139 (2018).
[39]A. Shariati, T. Ebrahimi, P. Babadinia, F. S. Shariati, and R. Ahangari Cohan, Sci. Rep. **13**, 4520 (2023).
[40]R. Krissak and M. Elgert, Adv. Mol. Imaging **3**, 37–42 (2013).
[41]M. Luo, J. Di, L. Li, Y. Tu, and J. Yan, Talanta **187**, 231–236 (2018).
[42]M. A. Motaleb, K. M. Attalah, H. A. Shweeta, and I. T. Ibrahim, BMC Chem. **17**, 21 (2023).
[43]B. A. Lakin, H. Patel, C. Holland, J. D. Freedman, J. S. Shelofsky, B. D. Snyder, K. S. Stok, and M. W. Grinstaff, J. Orthop. Res. **34**, 1130–1138 (2016).